crystals

MDPI

Article

Mechanical Performance of Ceria-Coated 3D-Printed Black Zirconia Cellular Structures After Solar Thermochemical CO/H_2 Fuel Production Cycles

Fernando A. Costa Oliveira [1,*], Manuel Sardinha [2], Joaquim M. Justino Netto [2], Miguel Farinha [2], Marco Leite [2], M. Alexandra Barreiros [1], Stéphane Abanades [3] and Jorge Cruz Fernandes [2]

[1] UME—Unidade de Materiais para a Energia, LEN—Laboratório de Energia, LNEG—Laboratório Nacional de Energia e Geologia I.P., Estrada do Paço do Lumiar 22, 1649-038 Lisboa, Portugal; alexandra.barreiros@lneg.pt
[2] IDMEC—Instituto de Engenharia Mecânica, Instituto Superior Técnico, University of Lisboa, Av. Rovisco Pais, 1049-001 Lisboa, Portugal; manuel.r.sardinha@tecnico.ulisboa.pt (M.S.); joaquim.netto@tecnico.ulisboa.pt (J.M.J.N.); miguel.farinha@tecnico.ulisboa.pt (M.F.); marcoleite@tecnico.ulisboa.pt (M.L.); cruz.fernandes@tecnico.ulisboa.pt (J.C.F.)
[3] PROMES—Processes, Materials, and Solar Energy Laboratory, CNRS—National Center for Scientific Research, 7 Rue du Four Solaire, Odeillo, 66120 Font-Romeu, France; stephane.abanades@promes.cnrs.fr
* Correspondence: fernando.oliveira@lneg.pt; Tel.: +351-218713431

Abstract

Solar fuels production requires developing redox active materials with porous structures able to withstand thermochemical cycles with enhanced thermal stability under concentrated solar irradiation conditions. The mechanical performance of 3D-printed, macroporous black zirconia gyroid structures, coated with redox-active ceria, was assessed for their suitability in solar thermochemical cycles for CO_2 and H_2O splitting. Experiments were conducted using a 1.5 kW solar furnace to supply the high-temperature concentrated heat to a windowed reaction chamber to carry out thermal redox cycling under realistic on-sun conditions. The ceria coating on ceramic structures improved the thermal stability and redox efficiency while minimizing the quantity of the redox material involved. Crushing strength measurements showed that samples not directly exposed to the concentrated solar flux retained their mechanical performance after thermal cycling (~10 MPa), while those near the concentrated solar beam focus exhibited significant degradation due to thermal stresses and the formation of $Ce_xZr_{1-x}O_2$ solid solutions (~1.5 MPa). A Weibull modulus of 8.5 was estimated, marking the first report of such a parameter for fused filament fabrication (FFF)-manufactured black zirconia with gyroid architecture. Failure occurred via a damage accumulation mechanism at both micro- and macro-scales. These findings support the viability of ceria-coated cellular ceramics for scalable solar fuel production and highlight the need for optimized reactor designs.

Keywords: thermochemical cycle; solar fuels; cellular materials; 3D printing; fused filament fabrication; black zirconia; crushing strength; Weibull modulus; elastic properties

Academic Editor: Jiamin Wu

Received: 5 June 2025
Revised: 2 July 2025
Accepted: 4 July 2025
Published: 8 July 2025

Citation: Costa Oliveira, F.A.; Sardinha, M.; Netto, J.M.J.; Farinha, M.; Leite, M.; Barreiros, M.A.; Abanades, S.; Fernandes, J.C. Mechanical Performance of Ceria-Coated 3D-Printed Black Zirconia Cellular Structures After Solar Thermochemical CO/H_2 Fuel Production Cycles. *Crystals* **2025**, *15*, 629. https://doi.org/10.3390/cryst15070629

1. Introduction

Global warming poses severe risks to ecosystems, economies, and public health, driving the urgent need to transition from fossil fuels to cleaner energy sources. Hydrogen (H_2), when produced sustainably, offers a carbon-free energy carrier and plays a crucial role in decarbonizing sectors where direct electrification is challenging [1].

Currently, H_2 is primarily used in oil refining and ammonia production [2], but its potential extends to heavy industry, such as steel, cement, and glass manufacturing, as well as long-haul transport and energy storage [3,4]. Despite its versatility, widespread adoption is limited by high production costs and infrastructure challenges [5].

A key pathway to clean hydrogen is through water electrolysis powered by renewables, yielding so-called "green hydrogen" (GH_2) [6]. However, as of 2019, 96% of hydrogen was still derived from fossil fuels, emitting circa 830 Mt CO_2 annually [7]. Increasing the GH_2 supply requires not only scaling up electrolyzer deployment, but also exploring alternative solar-driven production methods [8,9].

Among the diverse solar-driven hydrogen production pathways, photocatalytic, photoelectrochemical, photovoltaic (PV)–electrochemical, solar thermochemical, photothermal catalytic, and photobiological methods have emerged among the most intensively investigated. Except for PV, these technologies offer the potential for the direct conversion of solar energy into chemical energy, thus avoiding the need for intermediate electric production. Nonetheless, the limited long-term stability and durability of materials under actual operating conditions continue to pose significant barriers to large-scale industrial deployment. Addressing these issues is essential for improving system lifetimes, minimizing maintenance costs, and ensuring consistent H_2 yields under fluctuating solar irradiance and thermal cycling.

In this context, solar thermochemical hydrogen production has emerged as a potentially high-efficiency alternative. This process, which uses concentrated solar energy to drive two-step redox cycles involving metal oxides, allows for the direct conversion of solar energy into H_2 or syngas from H_2O and CO_2 splitting, without the need for the downstream separation of gas products (O_2 produced in reduction step and H_2 or CO in oxidation step) [10]. In theory, solar thermochemical cycles can achieve solar-to-fuel efficiencies exceeding 20%, which surpasses those achievable for photovoltaic electrolysis-based systems [11]. In practice, however, current systems developed at lab-scale demonstrate practical efficiencies of around 5%, and in some experimental setups, even lower (1.7%) [12].

Key redox-active materials under investigation for this process include ceria (CeO_2) and perovskite-based oxides (ABO_3 structure), which offer tunable redox properties suitable for high-temperature cycling [13]. Despite these advantages, significant challenges remain. Ceria suffers from sintering and a loss of performance after multiple redox cycles, while many perovskite oxides exhibit low re-oxidation yields and require further material design and optimization [14,15]. For instance, ceria achieves an increasing non-stoichiometry extent when heating up to around 1500 °C under low-oxygen partial pressures ($p(O_2) \approx 10^{-5}$ bar), where only ~3% of oxygen sites are vacant [16]. Under such demanding conditions, material microstructure degradation becomes a major limiting factor.

Furthermore, the levelized cost of hydrogen via thermochemical cycles currently ranges between USD 5 and USD 15 per kg H_2, compared to USD 1.03–2.16 per kg H_2 for steam methane reforming (SMR) [17,18]. The high capital and operational costs, largely due to extreme thermal requirements and material durability issues, continue to hinder commercial process viability.

Given these challenges, ongoing research is seeking to enhance the performance of redox materials, improve solar reactor designs, and increase the overall efficiency [19]. The future of solar thermochemical hydrogen production depends on overcoming these scientific and engineering barriers to realize its potential as a scalable, sustainable, and cost-effective hydrogen production pathway.

The additive manufacturing (AM) of ceramics has advanced significantly in recent years, with multiple process families now well-established for producing geometrically complex, high-performance ceramic components [20]. Key techniques include stere-

olithography (SLA), binder jetting, and direct ink writing, each offering distinct advantages, limitations, and application niches. Ullah et al. [21] review the major ceramic AM methods, highlighting laser powder-bed fusion and its typical defect mechanisms. Jasik et al. [22] compare photopolymerization and material extrusion, noting that while the former provides greater dimensional repeatability, the latter tends to yield nearly twice the compressive strength.

Among AM techniques, fused filament fabrication (FFF) has gained increasing attention for its simplicity, cost-effectiveness, and ability to produce geometrically complex components. While methods such as binder jetting and SLA typically offer a higher resolution and more homogeneous green bodies, FFF stands out as a robust and scalable approach for fabricating intricate lattice structures. Despite these advantages, ceramic FFF remains relatively underexplored, with only a limited number of studies reported to date [23]. Furthermore, the mechanical behavior of FFF ceramics is not yet well characterized, and existing data often show considerable variability in the strength and reliability [24–26]. This scatter is largely attributed to process-induced defects such as extrusion-related porosity, irregular bead geometry, and thermally induced cracks or blisters, all of which can degrade both the dimensional accuracy and mechanical integrity [27–29].

A previous study investigated the generation of solar fuels (CO and H_2) through thermochemical CO_2 and H_2O splitting, utilizing ceria-coated, 3D-printed black zirconia gyroid structures produced by an optimized FFF process [24]. Coating the gyroid structures with redox-active ceria offered several advantages, including reduced material usage, since only the surface coating participates in the redox reaction, as well as precise control over the coating thickness through layer adjustments. The 3D-printed zirconia support enhanced solid–gas interactions, with the surface reaction mechanism being typically the rate-limiting step in oxidation and provided thermal stability by buffering fluctuations in solar flux and minimizing thermal shock.

The coated structures were tested in a solar reactor under two-step thermochemical cycles at mean temperatures as high as 1400 °C. The results showed that 3D porous structures prepared by AM can improve the efficiency of solar fuel production compared to pure ceria. Nonetheless, signs of degradation were evident, especially in the upper section of the reactor cavity, where direct exposure to concentrated solar radiation induced the formation of $Ce_xZr_{1-x}O_2$ solid solutions at the interface between the ceria coating and the zirconia substrate. In contrast, samples located in the lower part of the reactor, shielded from direct radiation, retained their porous ceria structure and exhibited no significant mechanical degradation.

In the present study, data on the crushing strength before and after thermal cycling, along with measurements of the elastic properties of the gyroid struts, were collected to enable a more comprehensive characterization of the developed substrates.

Peak production rates of CO and H_2 in the solar reactor reached 5.4 and 1.9 mL min^{-1} g^{-1}, respectively, with fuel yields surpassing 0.2 mmol g^{-1} per cycle [24]. The fuel production performance remained stable over multiple redox cycles, with no significant loss in reactivity. The current study further investigates the retained crushing strength of thermally cycled samples to better understand their mechanical degradation. The results confirm that indirectly heated, coated zirconia gyroids maintain mechanical integrity, making them a promising solution for solar fuel generation via thermochemical processes.

2. Materials and Methods

2.1. Three-Dimensional Printing

The cubic gyroid samples used in this study were fabricated via FFF, using a 3 mol% yttria-stabilized ceramic-based filament, Zetamix Black Zirconia (3Y-ZrO_2), supplied by

Nanoe®. As reported by the manufacturer, the filament consists of 50 vol% submicron ceramic particles (<1.0 μm) dispersed in a thermoplastic binder matrix. The material's characteristic dark color results from the addition of cobalt iron oxide, $(Co,Fe)_2O_4$, with the final sintered components achieving a bending strength of at least 400 MPa [30].

Notably, printing with ceramics such as zirconia is a more demanding and complex process than that of conventional FFF thermoplastics, largely due to the filament's brittleness and the additional processing steps required, though processing guidelines for this specific filament material are provided in the manufacturer's datasheet [31]. Printing was performed using a Raise3D Pro2 dual-extruder 3D printer, with slicing conducted in IdeaMaker software (version 4.2.3). All samples were printed at an extrusion temperature of 180 °C, with a 0.4 mm nozzle diameter and a 0.2 mm layer height. The cooling fan was set to operate at full capacity throughout the process. No outer walls or contour perimeters were included in the slicing settings. Consequently, the samples were composed exclusively of infill paths, using a slicer predefined gyroid infill of 25%. These paths were deposited at a print speed of 10 mm s^{-1}, resulting in a volumetric extrusion rate ranging between 0.8 and 1.0 mm^3 s^{-1}. Figure 1 illustrates the printing process and the resulting printed component.

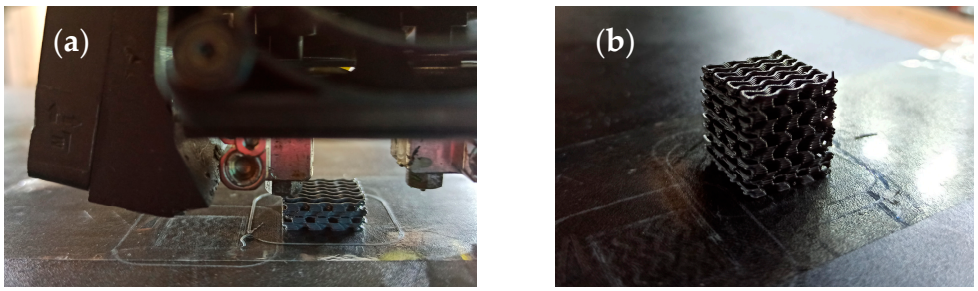

Figure 1. Production of the cubic gyroid samples on a Raise3D Pro2 3D printer using black zirconia. Mid-print process (**a**) and finished sample (**b**).

Following the 3D printing stage, the polymer binder was removed via a two-step debinding process. Initially, chemical debinding was performed by immersing the green parts in acetone at 40 °C for about 6 h, leading to a weight loss of 5–10%. This was followed by thermal debinding at approximately 500 °C over 30 h to eliminate the remaining binder. The samples were then sintered in a furnace at 1500 °C for 1.5 h. Controlled heating and cooling rates of 5 °C min^{-1} were applied, resulting in a total sintering cycle time of approximately 11 h. The experimental procedure, from sample production to the crushing tests, is illustrated in Figure 2.

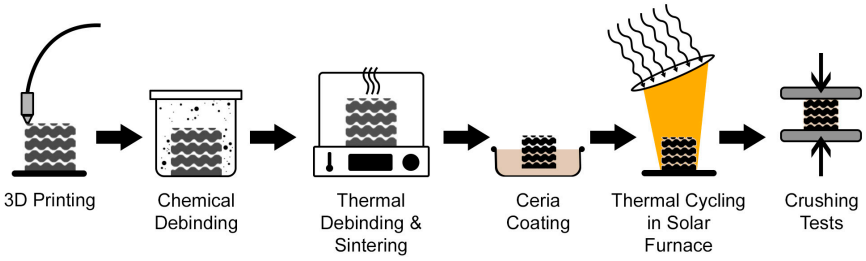

Figure 2. Overview of the experimental workflow, from 3D printing and debinding (chemical and thermal) to final sintering and mechanical (crushing) tests.

Figure 3 shows the as-printed and the sintered gyroid cuboid samples, with measurements showing a shrinkage of around 21% in the specimen's cross-section and a significantly lower shrinkage of approximately 15% along its height. This value is aligned

with the available literature [26,29] and was accounted for in the design and modeling stages of the cubic samples.

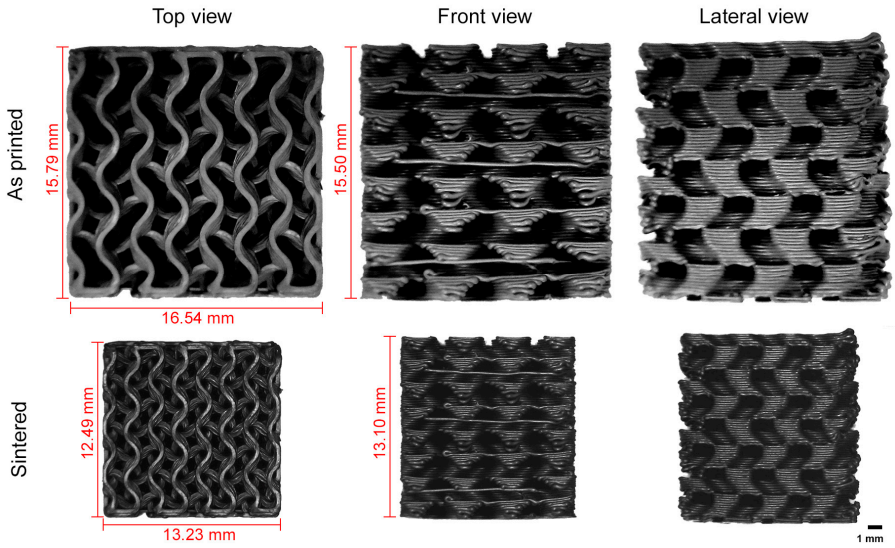

Figure 3. Representative top, front, and lateral views of the as-printed and sintered samples, showing maximum dimensions (in mm).

2.2. Thermochemical Redox Cycling Testing in a Solar Reactor

The thermochemical cycles were performed in the SUNFUEL reactor consisting of a windowed glass reaction chamber coupled to a vacuum pumping system, data acquisition systems, gases feeding, and respective gas analyzers (Figure 4). For this purpose, the reactor integrating the redox-active samples was mounted on a vertical axis Medium-Size Solar Furnace (MSSF) (2 m diameter parabolic concentrator) with a thermal power of 1.5 kW. Both B-type thermocouples and a solar-blind pyrometer (sensitive to wavelengths between 4.8 and 5.2 μm) were used for temperature measurements, employing a setup detailed in a previous study [24].

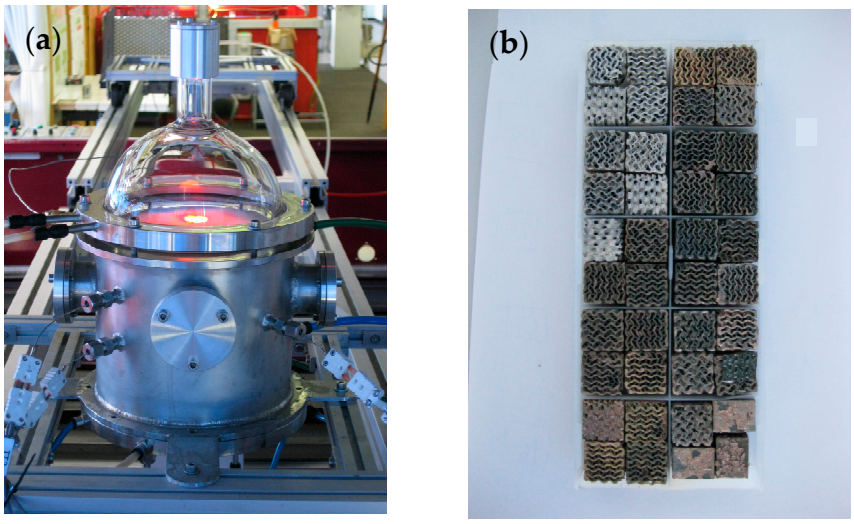

Figure 4. Overview of the SUNFUEL reactor upon cooling (**a**) and bird's-eye view of the exposed samples after thermochemical cycling under the conditions investigated (**b**).

Briefly, the cycles were carried out in flowing argon atmospheres (0.2 NL min^{-1} inside the inner alumina tube and 1.0 NL min^{-1} within the Pyrex chamber) during the reduction step (heating), and upon cooling, pure CO_2 (flowrate of 2 NL min^{-1}) was injected

to produce CO during the oxidation step. These tests were performed using Setup 1. During the oxidation step of the remaining cycles (Setup 2), H_2O vapor at a flow rate of 1.04 NL min^{-1}, diluted with 1.00 NL min^{-1} of argon, was introduced.

The heating and cooling times were set at 30 min (between T_{min} and T_{max}) and the soaking time was 15 min at T_{max}. Typically, the oxidation step lasted 6 min at T_{min} for CO_2 splitting and 14 min for H_2O splitting cycles.

The test conditions used are listed in Table 1.

Table 1. Solar thermochemical cycling conditions employed.

		Specimens				
		A	**B**	**C1**	**C2**	**D**
Setup 1	T_{max} (°C)	1525 ± 50 *	1450 ± 50	1375 ± 25		1300 ± 25
	T_{min} (°C)	650 ± 50 *	650 ± 50	650 ± 50		650 ± 50
	ΔT (K)	875	800	725		
	No. cycles	6	6	6		6
			+	+		+
Setup 2	T_{max} (°C)		1525 ± 50 *	1450 ± 50	1375 ± 25	1300 ± 25
	T_{min} (°C)		650 ± 50 *	650 ± 50	650 ± 50	650 ± 50
	ΔT (K)		875	800	725	650
	No. cycles		8	8	8	8
Total number of cycles		6	14	14	8	14

* Estimated values.

2.3. Elastic Moduli Measurements

To determine the elastic properties of the cubic sample struts, twelve discs (24.7 ± 0.2 mm in diameter and 2.0 ± 0.1 mm in thickness) were also fabricated via the FFF process and sintered under the same conditions described above. The dynamic Young's modulus (E) and shear modulus (G) at room temperature were measured using the impulse excitation method, in accordance with ASTM C1259-96 [32]. Measurements were performed with an acoustic testing device manufactured by IMCE NV (Genk, Belgium). The Poisson ratio, ν, was calculated according to:

$$\nu = \frac{E}{2G} - 1 \quad (1)$$

2.4. Crushing Tests

Crushing tests of the cubic samples were performed at room temperature using a mechanical testing machine (Instron Model 4302, Instron Corporation, Canton, MA, USA) equipped with a 10 kN load cell. The tests were conducted between flat steel plates at a crosshead speed of 0.5 mm min^{-1} [33]. To determine the "crushing strength" for each sample, the cross-sectional area was carefully measured, and the rupture stress was taken from the chart curve. To guarantee a more uniform loading, a compliant rubber with 2 mm in thickness was placed between the sample and the compressive stainless-steel plates. A minimum of 5 specimens were tested at each cycling condition.

2.5. Microstructural Evaluation

The fracture surfaces of the exposed samples were examined using a Philips XL30 FEG scanning electron microscope (SEM, Royal DutchPhilips Electronics Ltd., Amsterdam, The Netherlands) equipped with a field emission gun, operating at 10 kV in both secondary electron (SE) and backscattered electron (BSE) imaging modes.

3. Results and Discussion

3.1. Materials Characterization

The bulk density (ρ_b) of the cubes was determined to be 1.3 ± 0.1 Mg m^{-3}, corresponding to a porosity of circa 78% ($\varepsilon = 1 - \rho_b/\rho_r$). The real density ($\rho_r$) of the 3D-printed black zirconia filament struts, measured by helium pycnometry (AccuPyc 1300 model, Micromeritics Instruments Corporation, Norcross, GA, USA), was 5.96 ± 0.01 Mg m^{-3}. The area of each printed sample was measured using ImageJ software (version 1.54g, 2023; National Institutes of Health, Bethesda, MD, USA), with 10 measurements taken along each principal direction and 50 measurements taken for the strut thickness. The geometric dimensions of the cubic samples are listed in Table 2.

Table 2. Mean geometric dimensions (in mm) of the 3D-printed cubes.

	After Printing	After Sintering
Strut thickness	0.34 ± 0.03	0.26 ± 0.03
Height	15.50 ± 0.04	13.10 ± 0.04
Cross-section sides	(15.79 ± 0.05) × (16.54 ± 0.06)	(12.49 ± 0.02) × (13.23 ± 0.03)

The elastic properties of the disc samples are listed in Table 3.

Table 3. Elastic properties (Mean ± SD) of the 3D-printed black zirconia struts.

E (GPa)	G (GPa)	υ
150 ± 10	58 ± 4	0.28 ± 0.04

Young's modulus, a key parameter that defines the mechanical resistance of ceramic materials, represents the linear relationship between stress and strain within the elastic range. The values presented in Table 3 are slightly lower than typical values reported for Yttria-Stabilized Zirconia (YSZ), which are E = 205 GPa, G = 78 GPa, and ν = 0.31 [34], all obtained via the impulse excitation method. This reduction is attributed primarily to processing-induced defects, such as pores and microcracks, which are commonly associated with the debinding stage of the FFF process.

Many studies have investigated how porosity affects the Young's modulus of ceramics, resulting in various empirical models tailored to different material characteristics [35]. Among these, one of the most commonly used models is the one attributed to Spriggs [36], also known as the Duckworth–Knudsen equation [37], which is expressed as follows:

$$E = E_0 e^{-b\varepsilon} \quad (2)$$

where E_0 represents the Young's modulus of the fully dense, pore-free material; ε denotes the volume fraction of porosity; and b is an empirical porosity correction factor, typically determined from the slope of the linear region of the property–porosity relationship, often around a value of 4. The Duckworth–Knudsen equation is generally applied to denser materials and is valid over a relatively broad density range. Using E_0 = 150 GPa, b = 4, and ε = 0.78, the resulting modulus is E = 6.6 GPa.

Alternatively, the Gibson–Ashby model offers another approach for estimating the elastic moduli of porous structures [38]:

$$\frac{E}{E_0} \approx C_1 \left(\frac{\rho_b}{\rho_r}\right)^2 \quad (3)$$

Assuming $C_1 \approx 1$, the estimated Young's modulus is 7.1 GPa, which is 7.6% higher than the value predicted by the Duckworth–Knudsen model. This discrepancy is likely associated with the fact that cubic gyroid-based cellular structures cannot be classified as open-cell foams. Nonetheless, the estimated E modulus falls within the range forecast by both models, supporting their general applicability to such architected porous ceramics.

3.2. Crushing Behaviour

Typical compressive stress–strain curves of the samples are presented in Figure 5.

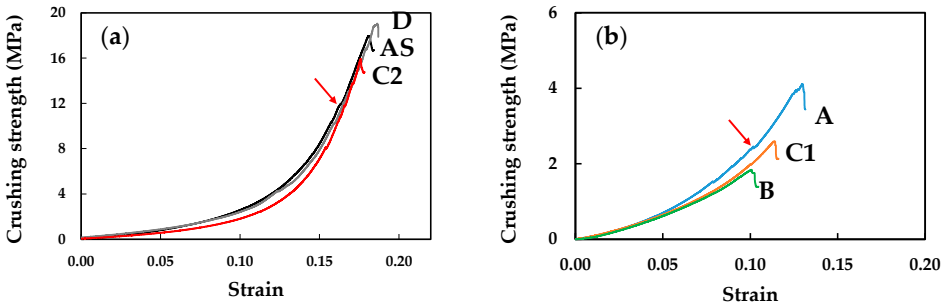

Figure 5. Representative compressive stress–strain curves for AS, C2, and D conditions (**a**), and A, B, and C1 conditions (**b**).

It is important to note that the propagation of a macrocrack through the gyroid structure significantly alters the shape of the stress–strain curve, as pointed out elsewhere [39]. This slope change—indicated by the arrows, as highlighted in the cases of AS and A samples—was, therefore, used as an indicator for determining the rupture strength (σ_{cs}). Notably, the maximum stress (σ_{max}) on the curve does not correspond to the actual failure of the samples tested in the as-sintered (AS) and D conditions. Table 4 presents the average values of σ_{cs} and σ_{max}. These values are lower than those reported previously [34]. Specifically, the crushing strength of as-sintered cubes with external walls (~35 MPa) is circa 3.5 times higher than the value obtained in the present study (~10 MPa), as shown in Table 4. Such a difference is expected, as the presence of dense external walls increases the overall stiffness of the cubic gyroid structure, leading to higher rupture strengths. In the present study, however, the geometry without external walls was deemed more suitable for the intended application as ceria-coated supports in solar-driven gas production via thermochemical cycling.

Table 4. Crushing strength data of as-sintered (AS) and different cycling conditions.

Specimens	$\sigma_{cs} \pm$ SD (MPa)	$\sigma_{max} \pm$ SD (MPa)	No. Specimens
A	1.62 ± 0.22	-	6
B	1.31 ± 0.30	-	5
C1	1.44 ± 0.23	-	6
C2	8.30 ± 0.37	-	5
D	9.40 ± 0.95	16.04 ± 1.70	8
AS	10.18 ± 1.31	15.94 ± 2.00	9

For samples exposed to temperatures not exceeding 1375 ± 25 °C (see Table 1), thermal cycling had little effect on the retained rupture strength (σ_{cs}), as shown in Table 4. This indicates that the ceria coating on the black zirconia gyroid structures performs effectively over the limited number of cycles tested. However, future work should address long-term durability to validate this hypothesis.

Data in Table 4 also indicate no statistical difference between the mean σ_{cs} values for both AS and D samples with a ~18.5% decrease observed for C2 samples. In contrast, for samples exposed to temperatures above 1375 ± 25 °C, the mean σ_{cs} decreased by ~85%. This substantial reduction is likely due to the formation of $Ce_xZr_{1-x}O_2$ solid solutions and thermal stresses that led to the cracking of struts and a loss of mechanical integrity.

Previous studies on zirconia gyroid structures with cell walls have shown that rapid temperature changes induce thermal stress distributions [39]. The intensity of these stresses is influenced by the heat transfer and thermal gradients between the sample's surface and its bulk. In such cases, the crushing strength decreased significantly from ~35 MPa to ~6 MPa (an ~83% drop) after 50 cycles at ΔT = 500 K [39]. This aligns with the drop in σ_{cs} shown in Table 4, from ~10 MPa to ~1.5 MPa (~85% decrease). These findings suggest that direct exposure to the concentrated solar beam may impose steep temperature gradients across the sample bulk, making indirect heating a potentially more suitable approach.

Brittle materials typically contain flaws of various sizes and types, resulting in significant variability in strength between samples. This variability is commonly expressed in terms of the failure probability. Since the exact strength distribution is generally unknown beforehand, an empirical model first introduced by Weibull [40] is frequently employed to describe it. Once the material's strength data are fitted to this distribution, failure probabilities can be predicted. If the predicted probability exceeds acceptable limits, it may compromise safety and necessitate either a redesign or the choice of a more suitable material. Typically, the two-parameter Weibull distribution is sufficient for reliable ceramic component design. This approach allows the estimation of the Weibull modulus (m) and the characteristic strength (σ_0, the scale parameter) from experimentally measured fracture stresses using linear regression. The procedure involves ordering the strength data in ascending order and assigning a corresponding failure probability to each sample. The following equation is then applied:

$$y = ln\left[ln\left(\frac{1}{P_S}\right)\right] = mln\sigma - mln\sigma_0 \quad (4)$$

This equation describes a linear relationship between y and $ln\sigma$, where the slope corresponds to the Weibull modulus, m. In this method, a failure probability is assigned to each test sample. The experimental survival probability, P_s, is commonly estimated as [41]:

$$P_S = 1 - \frac{(i - 0.5)}{n} \quad (5)$$

where i represents the rank of the fracture strength σ (with values arranged from weakest to strongest) and n is the total number of test samples. This estimator is known to provide the least biased estimate of the Weibull modulus m when $n > 20$ [41]. In recent years, the suitability of the Weibull distribution as the best fit for strength data has been questioned. The sample size plays a critical role in reliably distinguishing between different statistical distributions, such as normal, log-normal, gamma, or Weibull [42]. Within this framework, the Weibull modulus m quantifies the scatter of the data and is approximately inversely proportional to the coefficient of variation C_v, as expressed by [43]:

$$m \approx \frac{1.2}{C_v} \text{ with } C_v = \frac{SD}{\sigma_m} \quad (6)$$

where σ_m denotes the mean strength and SD represents the standard deviation. The data in Table 4 indicate that both samples tested under D conditions and in the AS state exhibited similar crushing strength values. This suggests that the types of flaws responsible for fracture are likely comparable. By combining the two datasets, the mean strength σ_m was

calculated to be 9.95 MPa with a standard deviation SD = 1.3 MPa for n = 17 samples. Using these values, the estimated Weibull modulus m is 9.2 (Equation (6)).

A Weibull plot (Figure 6) constructed from two sets of crushing data was fitted using linear regression, resulting in a Weibull modulus of 9.3, which is statistically the same as the value obtained from Equation (4).

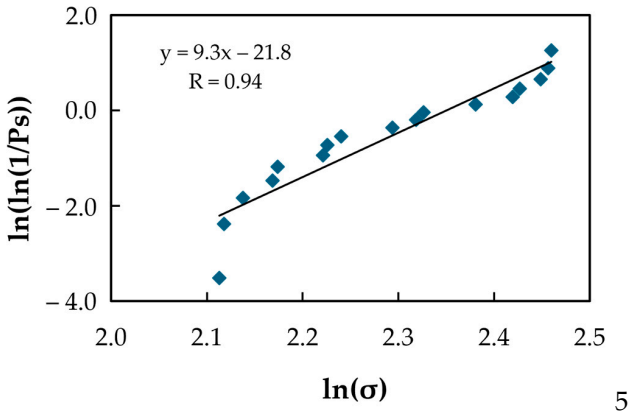

5

Figure 6. Weibull probability plot of crushing strengths of as-sintered (AS) and samples exposed under D condition.

For traditional ceramics, such as bricks, pottery, and glass, the m values are typically below three [44]. Therefore, the estimated m value in this study is circa three times higher, suggesting that the 3D printing process produces a narrower flaw size distribution compared to conventional ceramics. Conversely, engineering ceramics—with more tightly controlled manufacturing processes and typically fewer flaws—generally exhibit Weibull modulus values below 10 [44]. Thus, the estimated m value for the gyroid structure under investigation falls within the typical range for ceramic materials, indicating that the structure exhibits a relatively narrow flaw size distribution. Compared to dense zirconia tested under biaxial flexural strength, the Weibull modulus value of m = 9.5 aligns well with reported values ranging from 7.0 to 11.8, depending on the specific zirconia materials studied [45]. The characteristic strength σ_0 is determined from the intercept of the Weibull plot (equal to $-mln\sigma_0$) and found to be 10.5 MPa. This value corresponds to the stress level at which 63.2% of the samples are expected to fail, that is, when the failure probability reaches $1 - 1/e$.

For comparison, the Weibull parameters m and σ_0 were also estimated using the Maximum Likelihood Method in R software (version 4.5.0, The R Foundation for Statistical Computing, 2025). This method is recommended by a reference standard for reporting the uniaxial strength test data of advanced ceramics [46], which accounts for the sample size when estimating Weibull distribution parameters and their confidence bounds.

The initial result for m was 9.3. After applying unbiased corrections, the Weibull parameters were calculated as $\hat{m}_U$ = 8.5, with 90% confidence bounds of $\hat{m}_{upper}$ = 11.9 and $\hat{m}_{lower}$ = 6.1. The corresponding characteristic strength was σ_0 = 10.5 MPa, with bounds of $\sigma_{0,upper}$ = 11.0 MPa and $\sigma_{0,lower}$ = 9.9 MPa.

Data on the mechanical properties of black zirconia ceramics remain scarce, largely because traditional zirconia ceramics are mainly white or off-white, limiting their esthetic versatility and design flexibility [47]. The use of colored zirconia ceramics has broadened to applications such as dental restorative materials, decorative ceramics, mobile phone back panels, and other products [48]. About 25% of the pigments used in the ceramic industry are black, primarily derived from two main crystalline structures: hematite and spinel. Most of these black pigments originate from chrome–iron–nickel $(Ni,Fe)(Fe,Cr)_2O_4$ and iron–cobalt–chromite $(Fe,Co)(Fe,Cr)_2O_4$ black spinels [49,50]. Due to the scarcity and

high cost of cobalt oxide, alternative colorants to replace cobalt in zirconia ceramic such as TiO_2, $(Co_{1-x}Zn_x)(Fe_{1-y}Al_y)_2O_4$ have been explored [51,52]. An alternative method entails synthesizing oxygen-deficient black zirconia (ZrO_{2-x}) through controlled magnesiothermic reduction in a 5% H_2/Ar atmosphere, followed by HCl treatment to eliminate residual magnesium compounds, with the goal of enhancing solar light harvesting applications [53]. Despite these developments, limited mechanical properties of black zirconia are available: reference values of a bending strength of 1065 MPa, Vickers hardness of 9–12 GPa (14.3 ± 1.3 GPa, HV1 in the present study), and fracture toughness of 8–14 MPa $m^{½}$ were reported [54,55]. Recently, Justino Netto et al. [28] reported the fabrication of black zirconia gyroid structures utilizing the FFF technique, with variations in the unit cell size and wall thickness, employing a commercial black zirconia filament. The compressive strengths were observed to range from 7 to 37 ± 1 MPa, corresponding to an increase in the bulk density from 0.7 to 1.7 Mg m^{-3}. These findings align well with results reported by Costa Oliveira et al. [39] for similarly fabricated materials, albeit with different geometries (i.e., porous gyroid cubes with four face walls).

It is well established that failure in brittle cellular solids occurs through the catastrophic collapse of struts once a critical stress threshold is reached, resulting from a damage accumulation process [33]. Microstructural defects, such as pores and cracks within the struts, also significantly contribute to the failure of these highly porous cellular structures. This damage accumulation mechanism was further elucidated by Brezny and Green [56]. Due to the rigidity of the loading system and the imperfect flatness of the gyroid surfaces, a compliant layer was introduced to compensate for misalignments, thereby enabling a more uniform load transfer. Under compressive loading, the failure of these cellular materials was governed by progressive damage accumulation rather than by the sudden collapse of struts oriented perpendicular to the loading direction. It is hypothesized that damage accumulates on two scales: within individual struts and across the macrostructure. Fractures typically occurred on struts aligned perpendicular to the loading axis, indicating rupture predominantly by bending, as shown in Figure 7.

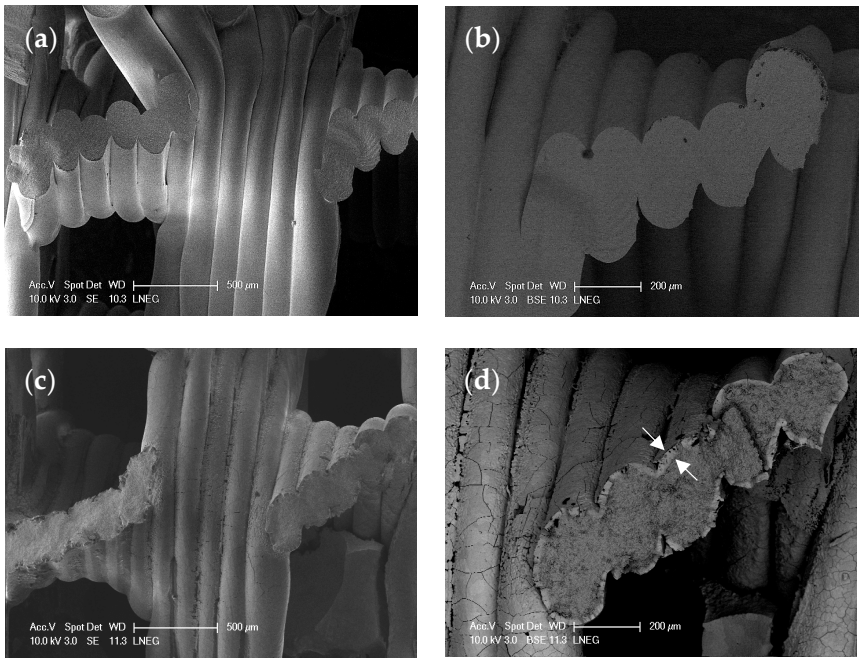

Figure 7. SEM micrographs of fractured filament surfaces acquired in secondary electron (SE) and backscattered electron (BSE) modes. (**a**,**b**) correspond to the as-sintered (AS) sample, showing no detectable coating. (**c**,**d**) show a sample tested under Condition A. Arrows indicate the coating thickness (~50 µm).

Notably, the ceria coating was uniformly distributed throughout the entire structure and demonstrated strong adhesion to the zirconia substrate, as clearly illustrated in Figure 7d. The coating thickness was generally in the range of 50–80 μm; however, in certain regions, it reached up to 500 μm (see the Supporting Data File, provided elsewhere, for detailed measurements) [24]. These variations are attributed to the complex geometry of the structures, the application of two coating layers to achieve sufficient ceria loading for testing, and limitations inherent to the dip-coating method.

The cracks observed on the surface of the coated struts are attributed to thermal expansion anisotropy arising from the formation of tetragonal $Ce_xZr_{1-x}O_2$ solid solutions at temperatures above 1400 °C [24]. For compositions with x in the range of 0.12–0.18, mean thermal expansion coefficients of $\alpha_a = 10.6 \times 10^{-6}$ K^{-1} and $\alpha_c = 13.5 \times 10^{-6}$ K^{-1} were determined in the temperature range from 294 to 1073 K [57]. These cracks likely developed during cooling and are predominantly intergranular, caused by the thermal expansion mismatch between the coating and the 3Y-ZrO_2 substrate.

4. Conclusions

This study offers new insights into the structural integrity of ceria-coated, macroporous, 3D-printed black zirconia structures following CO and H_2 fuel production through solar thermochemical cycles. Coating the 3D-printed black zirconia gyroid structures with redox-active ceria offered several advantages: reduced material usage (since only the surface coating participates in the redox reaction), enhanced solid–gas interactions (typically the rate-limiting step in oxidation), and improved thermal stability by buffering solar flux fluctuations, thereby minimizing thermal shock.

A key finding of this study is that samples indirectly exposed to the concentrated solar beam (condition D) maintained crushing strengths comparable to the as-sintered (AS) state, even after 14 cycles. This indicates that indirect heating may be a more effective strategy for preserving mechanical integrity, as it reduces thermal stress-induced damage and helps prevent the formation of undesired $Ce_xZr_{1-x}O_2$ solid solutions, which promote coating densification and lower redox efficiency. Based on the total porosity and the measured Young's modulus of the dense struts comprising the 3D-printed gyroid structures (150 ± 10 GPa), the effective modulus (overall stiffness) was estimated to be 6.9 ± 0.3 GPa using the Gibson–Ashby and Duckworth–Knudsen models.

Crushing strength data were analyzed using both the two-parameter Weibull distribution and the maximum likelihood method, yielding a Weibull modulus of 8.5 and σ_0 of 10.5 MPa within 90% confidence bounds. To the best of the author's knowledge, this is the first report of the Weibull modulus and shape parameters for black zirconia components fabricated via the FFF process featuring a gyroid cellular architecture. This advancement provides valuable insight into the mechanical reliability and strength distribution of additively manufactured black zirconia structures. A significant reduction from ~10 to 1.5 MPa (≈85%) in crushing strength was observed in samples located near the solar beam focus, i.e., closer to the top part of the reactor. This highlights the necessity for a redesigned reactor to achieve a more uniform temperature distribution throughout its height. Improved temperature control would help suppress the formation of $Ce_xZr_{1-x}O_2$ solid solutions and limit grain growth within the ceria coating, thereby enhancing the fuel conversion efficiency and increasing H_2/CO yields. Under compressive loading, the failure of the cellular structures occurred through a damage accumulation mechanism rather than through the catastrophic collapse of cells oriented perpendicular to the loading direction. It is hypothesized that damage develops on two scales: within individual struts and across the overall macrostructure. These observations underscore the importance of future research into the relationship between compressive mechanical behavior and

structural parameters—such as the cell size and wall thickness—to guide the design of materials with superior performance characteristics.

Author Contributions: Conceptualization, F.A.C.O. and J.C.F.; methodology, M.S., J.M.J.N., M.L., M.A.B., S.A. and J.C.F.; software, M.S., J.C.F. and M.L.; validation, F.A.C.O. and J.C.F.; formal analysis, F.A.C.O., J.M.J.N., M.S., M.F. and J.C.F.; investigation, F.A.C.O., M.S. and J.C.F.; resources, J.C.F.; data curation, F.A.C.O., M.S. and J.C.F.; writing—original draft preparation, F.A.C.O., M.S. and J.C.F.; writing—review and editing, F.A.C.O., M.S., J.M.J.N., M.F., M.L., M.A.B., S.A. and J.C.F.; visualization, F.A.C.O., M.S., J.M.J.N. and J.C.F.; supervision, F.A.C.O. and J.C.F.; project administration, F.A.C.O.; funding acquisition, F.A.C.O. and J.C.F. All authors have read and agreed to the published version of the manuscript.

Funding: This research was supported by the Fundação para a Ciência e a Tecnologia (FCT) through IDMEC, under LAETA Base Funding (DOI: 10.54499/UIDB/50022/2020). Additional funding from FCT for the National Research Infrastructure for Concentrated Solar Energy (INIESC) through contract ALT20-03-0145-FEDER-022113 is also gratefully acknowledged. Support from the European Commission through the SFERA-III project (Grant Agreement No. 823802) is duly recognized. This work was additionally funded by the European Union under the NextGeneration EU initiative, through Portugal's Recovery and Resilience Plan (PRR), within the scope of the PRODUTECH R3 project—Agenda Mobilizadora da Fileira das Tecnologias de Produção para a Reindustrialização (Project No. C645808870-00000067).

Data Availability Statement: The data presented in this study are available on request from the corresponding author.

Acknowledgments: F.A. Costa Oliveira gratefully acknowledges the CNRS-PROMES Laboratory for granting access to its research facilities. Sincere appreciation is also extended to Anita Haeussler for her valuable administrative support.

Conflicts of Interest: The authors declare no conflicts of interest.

References

1. Kovač, A.; Paranos, M.; Marciuš, D. Hydrogen in energy transition: A review. *Int. J. Hydrogen Energy* **2021**, *46*, 10016–10035. [CrossRef]
2. Zhu, Y.; Keoleian, G.A.; Cooper, D.R. The role of hydrogen in decarbonizing U.S. industry: A review. *Renew. Sustain. Energy Rev.* **2025**, *214*, 115392. [CrossRef]
3. Angelico, R.; Giametta, F.; Bianchi, B.; Catalano, P. Green hydrogen for energy transition: A critical perspective. *Energies* **2025**, *18*, 404. [CrossRef]
4. Gutowski, T.G.; Sahni, S.; Allwood, J.M.; Ashby, M.F.; Worrell, E. The energy required to produce materials: Constraints on energy-intensity improvements, parameters of demand. *Phil. Trans. R. Soc. A* **2013**, *371*, 20120003. [CrossRef] [PubMed]
5. Islam, A.; Alam, T.; Sheibley, N.; Edmonson, K.; Burns, D.; Hernandez, M. Hydrogen blending in natural gas pipelines: A comprehensive review of material compatibility and safety considerations. *Int. J. Hydrogen Energy* **2024**, *93*, 1429–1461. [CrossRef]
6. Fernández-Arias, P.; Antón-Sancho, Á.; Lampropoulos, G.; Vergara, D. On green hydrogen generation technologies: A bibliometric review. *Appl. Sci.* **2024**, *14*, 2524. [CrossRef]
7. IEA. *The Future of Hydrogen: Seizing Today's Opportunities*; International Energy Agency: Paris, France, 2019; Available online: https://www.iea.org/reports/the-future-of-hydrogen (accessed on 4 June 2025).
8. WEC. *Innovation Insights Brief: New Hydrogen Economy: Hope or Hype?* World Energy Council: London, UK, 2019. Available online: https://www.worldenergy.org/assets/downloads/WEInsights-Brief-New-Hydrogen-economy-Hype-or-Hope-ExecSum.pdf (accessed on 4 June 2025).
9. WEC. Hydrogen Insights 2024. World Energy Council. Available online: https://hydrogencouncil.com/wp-content/uploads/2024/09/Hydrogen-Insights-2024.pdf (accessed on 4 June 2025).
10. Wei, L.; Pan, Z.; An, L. Two-step thermochemical cycle for solar fuel production from H_2O and CO_2: Technological challenges and potential solutions. *Chem. Commun.* **2025**, *61*, 4897–4903. [CrossRef]
11. Kubicek, M.; Bork, A.H.; Rupp, J.L.M. Perovskite oxides—A review on a versatile material class for solar-to-fuel conversion processes. *J. Mater. Chem. A* **2017**, *5*, 11983–12000. [CrossRef]

12. Marxer, D.; Furler, P.; Takacs, M.; Steinfeld, A. Solar thermochemical splitting of CO_2 into separate streams of CO and O_2 with high selectivity, stability, conversion, and efficiency. *Energy Environ. Sci.* **2017**, *10*, 1142–1149. [CrossRef]
13. Haeussler, A.; Abanades, S.; Julbe, A.; Jouannaux, J.; Cartoixa, B. Solar thermochemical fuel production from H_2O and CO_2 splitting via two-step redox cycling of reticulated porous ceria structures integrated in a monolithic cavity-type reactor. *Energy* **2020**, *201*, 117649. [CrossRef]
14. Marxer, D.; Furler, P.; Scheffe, J.; Geerlings, H.; Falter, C.; Batteiger, V.; Sizmann, A.; Steinfeld, A. Demonstration of the entire production chain to renewable kerosene via solar thermochemical splitting of H_2O and CO_2. *Energy Fuels* **2015**, *29*, 3241–3250. [CrossRef]
15. Coronado, J.M.; Bayón, A. Catalytic enhancement of production of solar thermochemical fuels: Opportunities and limitations. *Phys. Chem. Chem. Phys.* **2023**, *25*, 17092–17106. [CrossRef] [PubMed]
16. Chueh, W.C.; Falter, C.; Abbott, M.; Scipio, D.; Furler, P.; Haile, S.M.; Steinfeld, A. High-flux solar-driven thermochemical dissociation of CO_2 and H_2O using nonstoichiometric ceria. *Science* **2010**, *330*, 1797–1801. [CrossRef]
17. Chen, C.; Jiao, F.; Lu, B.; Liu, T.; Liu, Q.; Jin, H. Challenges and perspectives for solar fuel production from water/carbon dioxide with thermochemical cycles. *Carb. Neutrality* **2023**, *2*, 9. [CrossRef]
18. Song, H.; Luo, S.; Huang, H.; Deng, B.; Ye, J. Solar-driven hydrogen production: Recent advances, challenges, and future perspectives. *ACS Energy Lett.* **2022**, *7*, 1043–1065. [CrossRef]
19. Abanades, S. Redox cycles, active materials, and reactors applied to water and carbon dioxide splitting for solar thermochemical fuel production: A review. *Energies* **2022**, *15*, 7061. [CrossRef]
20. Dadkhah, M.; Tulliani, J.-M.; Saboori, A.; Iuliano, L. Additive manufacturing of ceramics: Advances, challenges, and outlook. *J. Eur. Ceram. Soc.* **2023**, *43*, 6635–6664. [CrossRef]
21. Ullah, A.; Shah, M.; Ali, Z.; Asami, K.; Ur Rehman, A.; Emmelmann, C. Additive manufacturing of ceramics via the laser powder bed fusion process. *Int. J. Appl. Ceram. Technol.* **2025**, *22*, e15087. [CrossRef]
22. Jasik, K.; Kluczyński, J.; Miedzińska, D.; Popławski, A.; Łuszczek, J.; Zygmuntowicz, J.; Piotrkiewicz, P.; Perkowski, K.; Wachowski, M.; Grzelak, K. Comparison of additively manufactured polymer-ceramic parts obtained via different technologies. *Materials* **2024**, *17*, 240. [CrossRef]
23. Pandey, S.K.; Dixit, A.R. A multistage de-binding approach for material extrusion-based additively manufactured fabricated zirconia ceramics. *J. Korean Ceram. Soc.* **2025**, *62*, 553–566. [CrossRef]
24. Costa Oliveira, F.A.; Barreiros, M.A.; Sardinha, M.; Leite, M.; Fernandes, J.C.; Abanades, S. Thermochemical performance of ceria coated-macroporous 3D-printed black zirconia structures for solar CO/H_2 fuels production. *Int. J. Hydrogen Energy* **2025**, *100*, 477–490. [CrossRef]
25. Orlovská, M.; Hain, M.; Kitzmantel, M.; Veteška, P.; Hajdúchová, Z.; Janek, M.; Vozárová, M.; Bača, L. Monitoring of critical processing steps during the production of high dense 3D alumina parts using fused filament fabrication technology. *Addit. Manuf.* **2021**, *48 Pt A*, 102395. [CrossRef]
26. Truxová, V.; Šafka, J.; Sobotka, J.; Macháček, J.; Ackermann, M. Alumina manufactured by fused filament fabrication: A comprehensive study of mechanical properties and porosity. *Polymers* **2022**, *14*, 991. [CrossRef] [PubMed]
27. Schlacher, J.; Hofer, A.-K.; Geier, S.; Kraleva, I.; Papšík, R.; Schwentenwein, M.; Bermejo, R. Additive manufacturing of high-strength alumina through a multi-material approach. *Open Ceram.* **2021**, *5*, 100082. [CrossRef]
28. Justino Netto, J.; Sardinha, M.; Leite, M. Evaluating geometric conformity and compressive properties of black zirconia gyroid structures obtained through fused filament fabrication. *Int. J. Adv. Manuf. Technol.* **2025**, *138*, 1143–1157. [CrossRef]
29. Cano, S.; Gonzalez-Gutierrez, J.; Sapkota, J.; Spoerk, M.; Arbeiter, F.; Schuschnigg, S.; Holzer, C.; Kukla, C. Additive manufacturing of zirconia parts by fused filament fabrication and solvent debinding: Selection of binder formulation. *Addit. Manuf.* **2019**, *26*, 117–128. [CrossRef]
30. Cano, S.; Lube, T.; Huber, P.; Gallego, A.; Naranjo, J.A.; Berges, C.; Schuschnigg, S.; Herranz, G.; Kukla, C.; Holzer, C.; et al. Influence of the infill orientation on the properties of zirconia parts produced by fused filament fabrication. *Materials* **2020**, *13*, 3158. [CrossRef]
31. Black Zirconia Zetamix Filament. Available online: https://zetamix.fr/en/produit/black-zirconia-zetamix-filament/ (accessed on 28 May 2025).
32. *ASTM C1259-96*; Standard Test Method for Dynamic Young's Modulus, Shear Modulus, and Poisson's Ratio by Impulse Excitation of Vibration. ASTM International: West Conshohocken, PA, USA, 1996.
33. Costa Oliveira, F.A.; Dias, S.; Vaz, M.F.; Fernandes, J.C. Behaviour of open-cell cordierite foams under compression. *J. Eur. Ceram. Soc.* **2006**, *26*, 179–186. [CrossRef]
34. Giraud, S.; Canel, J. Young's modulus of some SOFCs materials as a function of temperature. *J. Eur. Ceram. Soc.* **2008**, *28*, 77–83. [CrossRef]
35. Rice, R.W. *Porosity of Ceramics*; Marcel Dekker Inc.: New York, NY, USA, 1998.
36. Pickup, R. Effect of porosity on Young's modulus of a porcelain. *Brit. Ceram. Trans.* **1997**, *96*, 96–98.

37. Lopes, M.A.; Silva, R.F.; Monteiro, F.J.; Santos, J.D. Microstructural dependence of Young's and shear moduli of P_2O_5 glass reinforced hydroxyapatite for biomedical applications. *Biomaterial* **2000**, *21*, 749–754. [CrossRef] [PubMed]
38. Costa Oliveira, F.A. Elastic moduli of open-cell cordierite foams. *J. Non-Cryst. Sol.* **2005**, *351*, 1623–1629. [CrossRef]
39. Costa Oliveira, F.A.; Sardinha, M.; Galindo, J.; Rodríguez, J.; Cañadas, I.; Leite, M.; Fernandes, J.C. Manufacturing and thermal shock resistance of 3D-printed porous black zirconia for concentrated solar applications. *Crystals* **2023**, *13*, 1323. [CrossRef]
40. Weibull, W.A. A Statistical Distribution Function of Wide Applicability. *ASME J. Appl. Mech.* **1951**, *18*, 293–297. [CrossRef]
41. Papargyris, A.D. Estimator type and population size for estimating the Weibull modulus in ceramics. *J. Eur. Ceram. Soc.* **1998**, *18*, 451–455. [CrossRef]
42. Nohut, S. Influence of sample size on strength distribution of advanced ceramics. *Ceram. Int.* **2014**, *40*, 4285–4295. [CrossRef]
43. Costa Oliveira, F.A.; Lopes, S.V.B.; Fernandes, J.C. Mechanical characterization of mortar beams. *Cienc. Tecnol. Mater.* **2017**, *29*, e172–e176.
44. Osuchukwua, O.A.; Salihia, A.; Ibrahima, A.; Audua, A.A.; Makoyoa, M.; Mohammedc, S.A.; Lawalc, M.Y.; Etinosad, P.O.; Isaace, I.O.; Onif, P.G.; et al. Weibull analysis of ceramics and related materials: A review. *Heliyon* **2024**, *10*, e32495. [CrossRef] [PubMed]
45. Roos, M.; Schatz, C.; Stawarczyk, B. Two independent prospectively planned blinded Weibull statistical analyses of flexural strength data of zirconia materials. *Materials* **2016**, *9*, 512. [CrossRef]
46. *ASTM C1239-06A*; Standard Practice for Reporting Uniaxial Strength Data and Estimating Weibull Distribution Parameters for Advanced Ceramics. ASTM International: West Conshohocken, PA, USA, 2006.
47. Yang, Y.; Hu, C.; Liu, Q.; Li, J. Research progress and prospects of colored zirconia ceramics: A review. *J. Adv. Ceram.* **2024**, *13*, 1505–1522. [CrossRef]
48. Costa, G.; Della, V.P.; Ribeiro, M.J.; Oliveira, A.P.N.; Monrós, G.; Labrincha, J.A. Synthesis of black ceramic pigments from secondary raw materials. *Dyes Pigm.* **2008**, *77*, 137–144. [CrossRef]
49. Calbo, J.; Sorlí, S.; Llusar, M.; Tena, M.A.; Monrós, G. Minimization of toxicity in nickel ferrite black pigment. *Br. Ceram. Trans.* **2004**, *103*, 3–9. [CrossRef]
50. Briod, R. Method of Manufacturing a Black Zirconia-Based Article and Black Zirconia-Based Decorative Article Notably Obtained by This Method. U.S. Patent 5711906A, 27 January 1998.
51. Fujisaki, H. Powder for Black Zirconia Sintered Body, Production Method Thereof, and Sintered Body Thereof. European Patent No. EP1857428A1, 21 November 2007.
52. Lv, H.; Bao, J.; Ruan, F.; Zhou, F.; Wang, Q.; Zhang, W.; Guo, W.; Zhang, Y.; Song, X. Preparation and properties of black Ti-doped zirconia ceramics. *J. Mater. Res. Technol.* **2020**, *9*, 6201–6208. [CrossRef]
53. Sinhamahapatra, A.; Jeon, J.-P.; Kang, J.; Han, B.; Yu, J.-S. Oxygen-deficient zirconia (ZrO_{2-x}): A new material for solar light absorption. *Sci. Rep.* **2016**, *6*, 27218. [CrossRef]
54. Zhao, L.; Wu, Y.; Guo, X.G.; Gao, H.; Lu, Y.; Liu, R. Preparation of colorful zirconia ceramics by liquid precursor infiltration. *Rare Met. Mater. Eng.* **2018**, *47*, 375–378. (In Chinese)
55. Ding, Y.; Wang, Q. Preparation and research of new black zirconia ceramics. *Sci. Rep.* **2024**, *14*, 3197. [CrossRef] [PubMed]
56. Brezny, R.; Green, D.J. Uniaxial strength behavior of brittle cellular materials. *J. Am. Ceram. Soc.* **1993**, *76*, 2185–2192. [CrossRef]
57. Scardi, P.; Maggio, R.D.; Lutterotti, L.; Maistrelli, P. Thermal expansion anisotropy of ceria-stabilized tetragonal zirconia. *J. Am. Ceram. Soc.* **1992**, *75*, 2828–2832. [CrossRef]